POLITECNICO DI TORINO
Repository ISTITUZIONALE

Unveiling the effect of Bi in ZnFe2O4 nanoparticles in electrochemical sensors

(Article begins on next page)

14 October 2024

Full Length Article

Unveiling the effect of Bi in ZnFe$_2$O$_4$ nanoparticles in electrochemical sensors

Mallikarjun Madagalam [a,b,c,*], Michele Rosito [a], Nicola Blangetti [a], Marco Etzi [d], Elisa Padovano [a,c], Barbara Bonelli [a,c], Sandro Carrara [b], Alberto Tagliaferro [a,c,e], Mattia Bartoli [c,d]

[a] *Department of Applied Science and Technology, Politecnico di Torino, Duca degli Abruzzi 24, 10129, Torino, Italy*
[b] *Bio/CMOS Interfaces Laboratory, École Polytechnique Fédérale de Lausanne, Rue de la Maladière 71b, 2000 Neuchâtel, Switzerland*
[c] *National Interuniversity Consortium of Materials Science and Technology Unit of Torino – Politecnico di Torino, Via Giuseppe Giusti, 9, 50121 Florence, Italy*
[d] *Center for Sustainable Future Technologies, Fondazione Istituto Italiano di Tecnologia, Via Livorno 60, 10144 Torino, Italy*
[e] *Faculty of Science, OntarioTechU, 2000 Simcoe Street North, Oshawa, Ontario L1G 0C5, Canada*

ABSTRACT

This work investigates the effect of the inclusion of Bi^{3+} ions in ZnFe$_2$O$_4$ nanoparticles on electron transfer at the electrochemical interface. ZnBi$_x$Fe$_{2-x}$O$_4$ (x = 0, 0.5, 1, 2) nanomaterials are synthesized and the impact of Bi^{3+} ions on the chemical features of ZnFe$_2$O$_4$ nanoparticles is studied by using different materials' characterization techniques. The effect of the change in the chemical composition of ZnFe$_2$O$_4$ nanoparticles on the electrochemical sensing performance is extensively studied and correlated with the electrochemical sensitivity and kinetic rate constant. Screen-printed electrodes functionalized with ZnBi$_x$Fe$_{2-x}$O$_4$ nanomaterials have an excellent enhancement of electrochemical sensing performance towards paracetamol, as a test molecule, compared to the carbon electrodes. The highest sensitivity (37.8 $\pm$ 0.2 μA/mM) and the best kinetic rate constant (13.1 $\pm$ 2.8 ms^{-1}) are achieved by the ZnFe$_2$O$_4$ sensor, while the ZnBi$_2$O$_4$ sensor achieved a sensitivity of (23.5 $\pm$ 0.6) μA/ mM with a kinetic rate constant of (0.45 $\pm$ 0.16) ms^{-1}. The ZnFe$_2$O$_4$ sensor is found to have a direct electron transfer, whereas the other sensors participate in a surface state-mediated electron transfer at the electrochemical interface. This research shows a clear path to the potential applications of spinel oxide-based electrochemical sensors for specific drugs or molecules detection.

1. Introduction

Transition multi-metal oxide nanomaterials have excellent potential in various applications due to the availability of multiple levels of freedom in the nanomaterial design. However, the fundamental awareness of different activities (especially electrocatalytic activity) of these oxides is limited because of the high complexity related to the presence of multi-metals in their composition [1]. The level of complexity rises when the crystal structure has more than one site for metal occupancies, as it occurs for instance in the cubic spinel crystal system [2,3]. Understanding the origin of the electrochemical/catalytic activity in such materials is rather challenging. Due to the presence of more than one metal with different oxidation states of the metal ions in the system, the spinel multi-metal oxides have shown excellent potential in electrocatalytic oxygen evolution reactions,[1,4] electrochemical

sensors,[5,6] photocatalytic activities,[3,7] and energy applications such as supercapacitors[8,9] and batteries [2,10,11].

The spinel structure typically provides two different sites (tetrahedral 'Td' and octahedral 'Oh') for metals to occupy. Different metals prefer to occupy different sites based on their oxidation states and crystal field stabilization energies of the metal ions. Based on the occupied metal ions the spinel system is divided into normal spinel, inverse spinel, and mixed spinel systems [5]. Normal spinel is the simple arrangement of metal ions with bivalent cations placed in the 'Td' sites and trivalent cations placed in the 'Oh' sites formed by the oxygen anions. Based on the trivalent cation in the composition of the spinel they are referred to as ferrites with Fe(III), cobaltites with Co(III), manganites with Mn(III), and chromites with Cr(III) ions.

Spinel nanomaterials can be synthesized using different techniques based on the application requirements. For example, precipitation and

---

crystallization,[12] one-step hydrothermal reaction,[13] micro-emulsion method,[14] sol–gel synthesis,[15] and combustion techniques[5] are widely used.

Among the different classes of spinel nanomaterials, ferrites are of great interest due to their magnetic, electrical, and optical properties [5,14,16,17]. One of the well-known ferrites is $ZnFe_2O_4$ (zinc ferrite); its properties can be enhanced/modified by partially substituting iron with other ions into the crystal system. This can either sustain the same spinel type or be modified into another spinel type based on the type of cations introduced.

We have studied these structural transitions by introducing Ni^{2+} ions into the $ZnFe_2O_4$ crystal system and clearly demonstrated that the amount of Ni^{2+} ions gradually changed the normal spinel $ZnFe_2O_4$ into an inverse spinel $NiFe_2O_4$ through mixed spinel phases ($Zn_xNi_{1-x}Fe_2O_4$). These structural transitions have significantly enhanced the electrochemical sensing performance of the spinel-based nanomaterials functionalized sensors [5]. In another case, when Cr^{3+} ions are introduced, we observed that the phase has not changed from normal spinel as there is a huge preference for tetrahedral and octahedral sites for Zn and Cr, respectively, due to their respective crystal stabilization energies. Though the introduction of Cr^{3+} ions leads to the formation of the same structural phase there are significant changes in the electrochemical performance of the nanomaterials due to slight changes in the mole fraction (x) of the composition and differences in the ionic radii of Cr^{3+} and Fe^{3+} ions. Even slight differences at the electrochemical interface in any form can show significant differences in the sensor performance as the electrochemical reactions are very sensitive to any kind of change at the interface [18,19].

Paracetamol is used as a model-molecule of therapeutic compounds. It is also known as acetaminophen is a widely used analgesic, antipyretic drug to treat fever, pain, and headache [20,21]. Usually it is safe when it is used as directed within limits but the overdosage can cause severe liver damage [21,22]. Due to this reason monitoring or detecting the paracetamol levels is very important, there are various sensing techniques to detect and monitor the paracetamol concentration levels. There are various analytical methods proposed among which electrochemical sensing method is the more reliable and cost-effective method [23]. Since paracetamol is an electroactive molecule, it has been widely used in testing different types of new electrochemical sensors which employed various metal oxides based nanomaterials [24–27]. Spinel metal oxides-based nanomaterials have also been used in electrochemical sensing of paracetamol such as La-doped $CuFe_2O_4$,[28] clay $MnFe_2O_4$ nanocomposites,[29] $MnFe_2O_4$,[30] $NiFe_2O_4$,[5,31,32] $ZnFe_2O_4$,[5,33] and $CoFe_2O_4$.[34]

Another interesting spinel nanomaterial is obtained by inserting bismuth in the spinel structure producing $ZnBi_2O_4$. $ZnBi_2O_4$ is mainly used for photocatalytic applications in combination with other oxides to form p-n junction to reduce the recombination rates. It is used as a photo-catalyst for degradation of organic pollutants in junction with Bi_2O_3,[35] ZnO,[36] and as an enhanced photocatalyst under visible light with TiO_2 QDs [37]. However, there is not much research available in the literature about the electrocatalytic applications of bismuthate, even though a similar mechanism should be involved in both phenomena. Therefore, our interest is to study the electrochemical sensing behaviour of bismuthates and in combination with ferrites to understand the synergic effect on electrochemical sensing [19].

This work focuses on the effect of the partial substitution of Fe^{3+} ions with Bi^{3+} ions in the crystal structure of $ZnFe_2O_4$ nanoparticles. Bi^{3+} ions are gradually introduced into the composition of $ZnFe_2O_4$ and $ZnBi_xFe_{2-x}O_4$ (x = 0, 0.5, 1, 2) nanomaterials are synthesized by auto-combustion technique. Commercially available screen-printed carbon electrodes are functionalized with $ZnBi_xFe_{2-x}O_4$ nanomaterials to fabricate the new spinel oxide-based electrochemical sensors. Cyclic voltammetry is used to electrochemically characterize the sensors in the detection of paracetamol as a test molecule. Chemical features of the nanomaterials are deeply discussed and correlated with the

electrochemical parameters such as sensitivity and kinetic rate constant. The energy band gap of the nanomaterials is computed and correlated with the experimental electrochemical peak potentials to understand the electron transfer mechanism at the electrochemical interface.

2. Materials and methods

2.1. Chemicals

$Zn(NO_3)_2 \cdot 6H_2O$ (Zinc nitrate), $Fe(NO_3)_3 \cdot 9H_2O$ (Iron nitrate), $Bi(NO_3)_3 \cdot 9H_2O$ (Bismuth nitrate), $C(NH_2)_2O$ (Urea), $C_4H_{10}O$ (Butanol), and paracetamol powder are purchased from Sigma Aldrich and used without any further purification.

2.2. Material synthesis

Adopted from the literature, a simple, single-step, and cost-effective auto-combustion method is used for the material synthesis [5,38]. The combustion method was widely used in the production of Bi in $ZnFe_2O_4$ nanomaterials [39–42]. Depending on the composition of the material, metal nitrate/s (oxidizing agent) are mixed with urea (reducing agent acts as a fuel) in correct stochiometric proportions (1:1 mole ratio of oxidizer to reducer) to prepare a redox mixture. The newly prepared redox mixture is kept in a graphite reactor which was inserted into a furnace. The furnace is heated up to 600 °C and the product is annealed at 600 °C for 1 h then it is cooled until it reaches the room temperature and grounded to obtain the final spinel-oxide nanomaterials. The synthesis scheme is shown in Fig. 1.

2.3. Physicochemical characterization

Field emission scanning electron microscopy (FESEM) is conducted utilizing the Zeiss SupraTM 50 (Oberkochen, Germany) to examine the nanomaterial's morphology. Micro-Raman spectroscopic measurements are performed by employing the Renishaw, inVia Raman Microscope to identify the molecular vibrations or get structural information of the materials. The phases and crystal structure of the materials are determined by X-ray diffraction (XRD) using a Panalytical Empyrean diffractometer (Malvern Panalytical, Malvern, UK). The analysis is carried out using a time step of 60 s and a step size of 0.013°/s, covering a 2θ range from 20° to 70°, in a Bragg-Brentano geometry and with a radiation source of Cu Kα (λ = 1.5418 \AA) at 40 kV and 40 mA. A Cary 5000 ultraviolet visible near infrared (UV–Vis-NIR) spectrophotometer (Varian Instruments, Mulgrave, Australia) equipped with a diffuse reflectance (DR) system is employed for UV–visible investigations. X-ray photoelectron spectroscopy (XPS) experiments are carried out in a PHI 5000 Versaprobe spectrometer equipped with a monochromatic Al Kα (1486.6 eV) X-ray source. An Ar ion gun and an electron gun are used for charge compensation. Binding energy calibration is performed by setting the adventitious C sp^3 component at 284.8 eV. Pass energies are set at 187.85 and 23.5 eV for the acquisition of survey and high-resolution scans, respectively. XPS spectra are processed using CasaXPS software (v2.3.23, Casa Software Ltd).

2.4. Electrodes modification

The electrochemical sensing elements (Electrochemical sensor) are composed of screen-printed electrodes with an Ag/AgCl reference electrode (RE), a carbon counter electrode (CE), and a carbon working electrode (WE) (area 0.12 cm^2). To prepare the nanomaterial suspensions, 3 mg material is added to 1 mL (3:1 material to solvent ratio) of butanol. The mixture is then homogenized in an ultrasonic bath. The drop-casting technique is used for electrodes modification. The sensors are modified after dropping 5 μL of nanomaterial suspension on top of the WE and permitted to dry at 27 °C (room temperature) for 24 h.
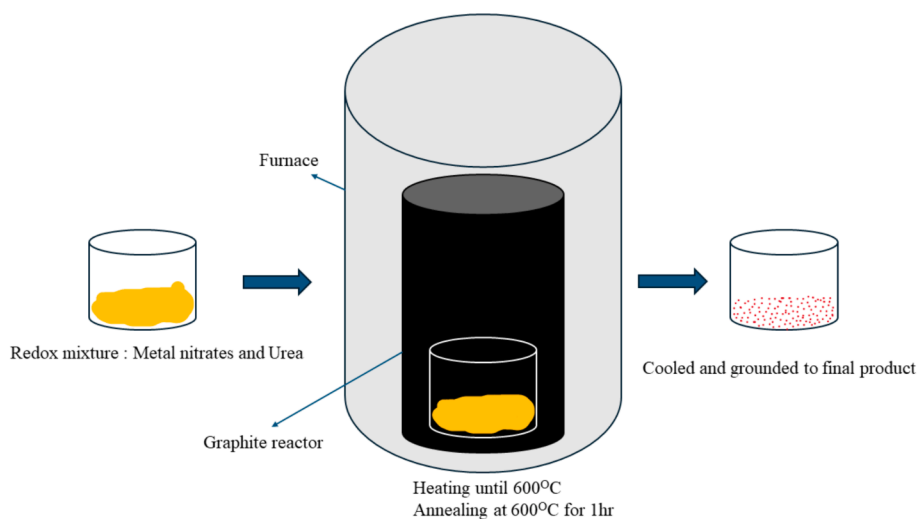
Fig. 1. Auto combustion synthesis scheme.

2.5. Electrochemical measurements

Cyclic voltammetry (CV) experiments are conducted using a Bio-logic SP-300 potentiostat to detect paracetamol in a 0.1 M PB (Phosphate Buffer) solution at pH 7 (electrolytic solution). The sweeping voltage ranged from –0.6 to + 0.8 V (versus Ag/AgCl). Cyclic voltammograms are acquired by applying 100 μL of electrolytic solution onto the electrochemical sensor. Redox currents and potentials are analyzed after getting rid of the non-Faradaic current through background correction using peak analysis in EC-Lab software. CV measurements are performed by varying the scan rate from 50 to 300 mV/s (in increments of 50 mV/s) to investigate the electrochemical interface. Additionally, CV experiments are conducted at different concentrations of paracetamol, ranging from 0.5 mM to 3 mM with intervals of 0.5 mM, to establish
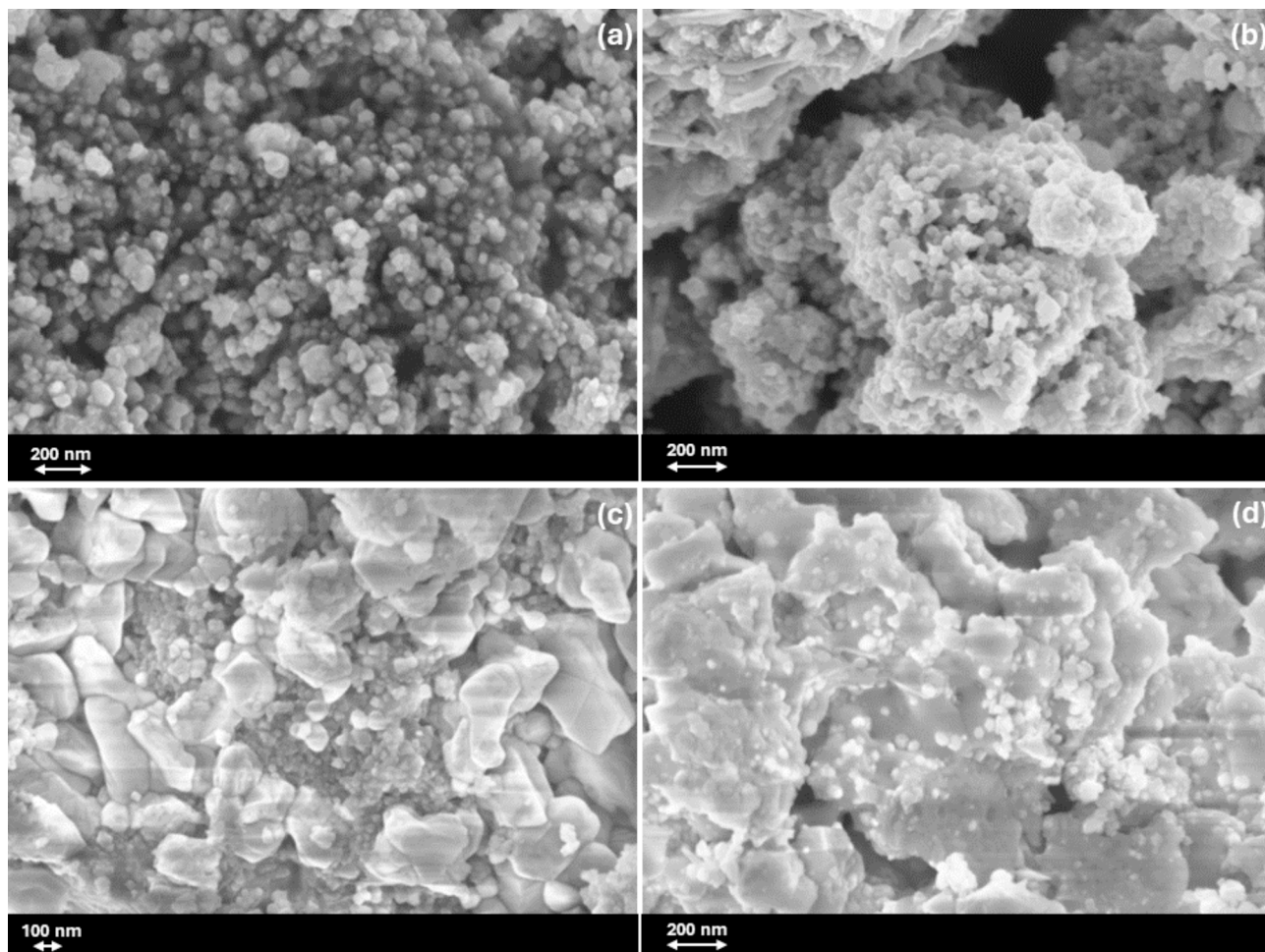

Fig. 2. FE-SEM images of (a) $ZnFe_2O_4$, (b) $ZnBi_{0.5}Fe_{1.5}O_4$, (c) $ZnBiFeO_4$, and (d) $ZnBi_2O_4$ at a magnification of 50x.

the calibration of the sensors. Electrochemical impedance spectroscopy (EIS) is performed in the frequency range of 0.1 Hz to 100 kHz with 10 points per decade with an amplitude of 5 mV.

3. Results and discussion

3.1. Morphological and structural characterization

Fig. 2 shows the FESEM images of $ZnBi_xFe_{2-x}O_4$ (x = 0, 0.5, 1, 2) materials. From Fig. 2(a), we observe highly nanostructured particles with spherical shape for pure $ZnFe_2O_4$ material (x = 0). In Fig. 2(b) to (d) we observe two different particle morphologies as the amount of Bi increases from x = 0.5 to 2. Some of the particles become larger and their shape changes from quasi-spherical to patch-like morphology as we increase the amount of Bi. The degree of nanostructured particles has decreased as we completely replaced Fe(III) with Bi(III) in the composition of the materials. From the FESEM images, it is evident that most of the particles have sub-micrometer (>100 nm and < 1 μm) dimensions and some particles retained the spherical shape with nanometer size as we move from x = 0 to 2.

In Fig. 3, the XRD patterns of $ZnBi_xFe_{2-x}O_4$ (x = 0, 0.5, 1, 2) are shown. For x = 0, the diffraction pattern fully matches with the normal spinel Franklinite (zinc iron oxide) (ICDD ref. code 01–089-4926), while for x = 2, the XRD pattern is in good agreement with cubic bismuth zinc oxide (ICDD ref. code 01–077-0569). The intermediate compositions (x = 0.5, 1) exhibit a hybrid pattern, with peaks attributable to both zinc-iron oxide and bismuth-zinc oxide as depicted in Fig. 3.

In all patterns, some minor peaks are observed between 30° and 37°: we assign these peaks to zinc oxide (ICDD ref. code 01–080-0075) and iron oxide (ICDD ref. code 01–085-0987) since their position coincides with that of the most intense peaks of these two phases[5]. The zinc oxide and the iron oxide are possible as secondary phases due to the reactants used in the synthesis process.

Scherrer's method is applied to calculate the crystallite size of the particles on seven major peaks [5]. The crystallite size of the materials is reported in Table 1. The crystallite size varies from material to material as the composition of the material changes, in agreement with previous literature [5]. For x = 0.5, the introduction of Bi^{3+} into the $ZnFe_2O_4$ structure has a significant effect on the lattice strain, while it increases slightly for x = 1. The ionic size of Bi^{3+} (103 pm)[43] is higher than that of Fe^{3+} (64.5 pm),[43] and this might lead to a higher strain as the Bi content increases. For x = 2, when Fe(III) is completely replaced with Bi

Table 1
The crystallite size and microstrain of $ZnBi_xFe_{2-x}O_4$ (x = 0, 0.5, 1, 2) nanomaterials.

Material	D (nm)	Strain
$ZnFe_2O_4$	35 ± 3	0.003 ± 0.002
$ZnBi_{0.50}Fe_{1.50}O_4$	40 ± 20	0.003 ± 0.001
$ZnBiFeO_4$	31 ± 5	0.004 ± 0.001
$ZnBi_2O_4$	49 ± 12	0.002 ± 0.001

(III) the strain is reduced compared to the $ZnFe_2O_4$ system. This could be due to the better matching of the site space to the ionic size of Bi^{3+}.

3.2. Spectroscopic characterization

As shown in Fig. 4, all the bands below 220 cm^{-1} for $ZnBi_xFe_{2-x}O_4$ (x = 0.5, 1, 2) materials are assigned to the Bi and O framework as in cubic Bi_2O_3 [44]. The band above 600 cm^{-1} is attributed to the A_{1g} symmetry of the spinel structure whereas the band around 445 cm^{-1} is assigned to the $T_{2g}(3)$ symmetry of the spinel. Raman bands of materials with x = 0.5, 1, 2 around 310 and 520 cm^{-1} are also assigned to Bi and O bonds related to the Cubic Bi_2O_3 phase. Another band around 345 cm^{-1} is assigned to the $T_{2g}(2)$ mode of the spinel for materials with x = 0.5, 1 while this mode is not observed for x = 2. The band around 250 cm^{-1} could be attributed to the shifted E_g mode of the spinel due to local variations because of the presence of both Fe and Bi in the crystal structure or, alternatively, could be another band related to the cubic Bi_2O_3 as there is a small difference of 30 cm^{-1} with the E_g mode of the spinel material with x = 0 as demonstrated previously [5]. For x = 2 material the band around 375 cm^{-1} is related to the Zn-O bonding as in ZnO [45].

To evaluate the surface states and oxidation states of the elements in the materials $ZnBi_2O_4$ and $ZnBiFeO_4$, XPS high-resolution (HR) spectra of the elements are recorded. Fig. 5(a) shows the HR spectrum of Zn 2p with peaks at binding energies (BE) of 1021.5 eV and 1044.6 eV related to Zn $2p_{3/2}$ and Zn $2p_{1/2}$ states. The position of the peaks points toward the presence of Zn^{2+} [5]. HR spectra of Bi 4f region are shown in Fig. 5 (b), with Bi 4f orbital splitting into Bi $4f_{7/2}$ and Bi $4f_{5/2}$. The components at 158.5 eV and 163.9 eV are assigned to octahedral Bi^{3+} while those at 160 and 165 eV to tetrahedral Bi^{3+}, confirming the presence of Bi^{3+} at two sites in the main spinel phase.[9,46] The core level spectrum of Fe 2p orbital has a doublet at 711.5 eV and 725.1 eV corresponding to Fe $2p_{3/2}$ and Fe $2p_{1/2}$, respectively, with complementing shake-up satellites at 718.5 and 732.8 eV, as depicted in Fig. 5(c). The peaks of Fe $2p_{3/2}$ and
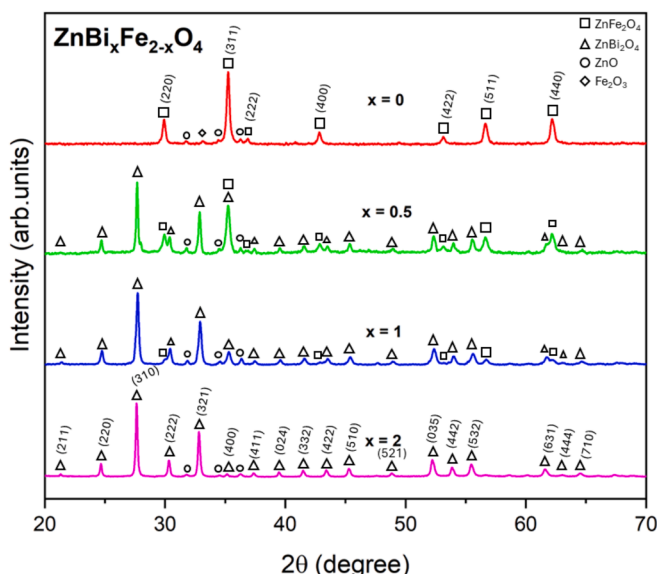
Fig. 3. XRD patterns of $ZnBi_xFe_{2-x}O_4$ (x = 0, 0.5, 1, 2) nanomaterials.

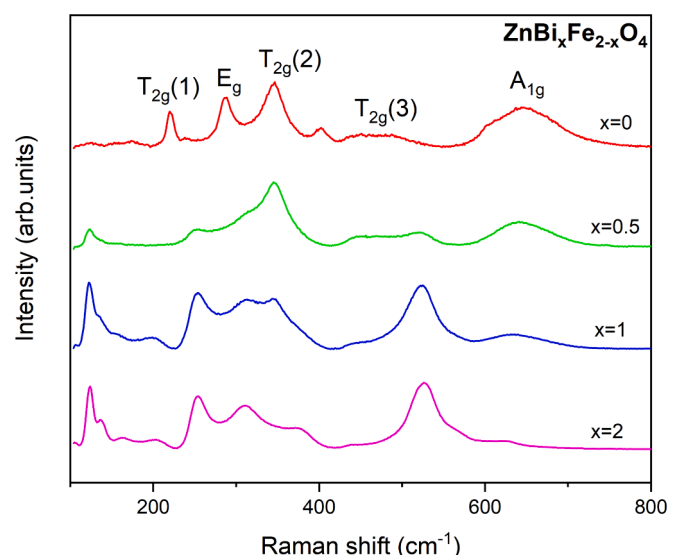**Fig. 4.** Raman spectra of $ZnBi_xFe_{2-x}O_4$ (x = 0, 0.5, 1, 2) nanomaterials.
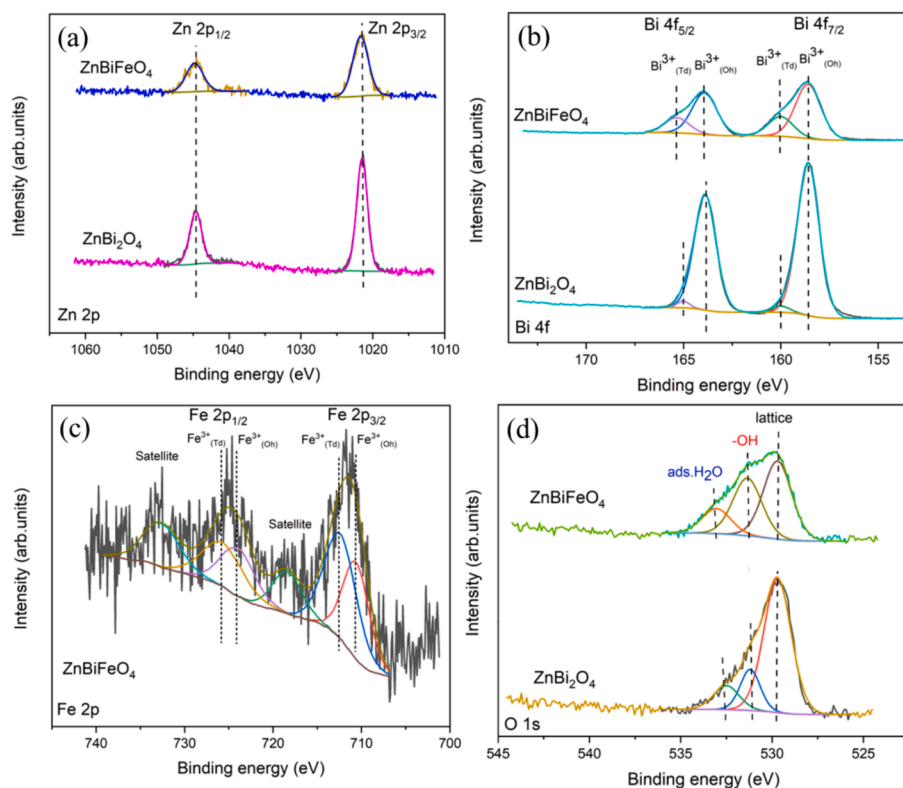
Fig. 5. High-resolution XPS spectra of (a) Zn 2p, (b) Bi 4f, (c) Fe 2p, (d) O 1 s regions.

Fe $2p_{1/2}$ are deconvoluted using two different components corresponding to octahedral (710.8 and 724.1 eV) and tetrahedral (712.6 and 725.9 eV) Fe^{3+} in the spinel crystal structure [9]. XPS spectra of O 1 s are shown in Fig. 5(d); fitting is performed using three components ascribed to oxygen in the main lattice phase (~529.6 eV), in hydroxyl groups (~531.3 eV), and adsorbed water (~533.1 eV) [5,47,48]. The atomic concentrations derived from the survey spectra of the elements for materials with x = 1 and 2 are evaluated and reported in Table S1, supporting information. The ratio of the atomic percentage of Bi to Zn is about 2.29 (x = 2) and 1.96 (x = 1); in the case of x = 1 the ratio is close to the expected ratio of 2. By combining these results with those obtained by XRD, we confirm the presence of the cubic spinel phase of $ZnBi_2O_4$. Moreover, Bi^{3+} ions preferentially occupy the octahedral sites in the absence of Fe^{3+} ions in the structure referring to a normal spinel structure from Fig. 5(b). For x = 2, the ratio is much higher than expected; this might be due to surface enrichment in Bi. As reported in Figure S1 (supporting information), other than the expected elements present in the oxides we found only the presence of adventitious carbon on the surface.

Diffuse reflectance UV visible (DR UV–vis) spectra of $ZnBi_xFe_{2-x}O_4$ (x = 0, 0.5, 1, 2) materials are reported (F(R) Kubelka-Munk vs. wavelength) in Fig. 6 [49]. Zinc ferrite ($ZnFe_2O_4$) showed three main bands with maxima at ca. 800 nm, 500 nm and 300 nm. The most intense band, with maximum at 300 nm, can be ascribed to the $O^{2-} \rightarrow Fe^{3+}$ charge transfer transition (CT), usually giving rise to an intense absorption [50]. As expected, the intensity of this band decreases as the content of Bi increases, and, accordingly, cannot be appreciated in the spectra of the $ZnBiFeO_4$ and $ZnBi_2O_4$ samples, which show an intense absorption below 400 nm, with a different shape. The band at 500 nm can be assigned, according to the literature, to an internal crystal field transition (CF) $^6A_2 \rightarrow {}^4A_1$ ($^4E(^4G)$) associated with octahedral Fe^{3+} sites [50]. Another evidence of the presence of octahedrally coordinated Fe^{3+} sites is the band at 800 nm (inset to Fig. 6), which was assigned to the $^6A_2 \rightarrow {}^4T_1$ (4G) transition of octahedral Fe^{3+} sites. [5,51] This band was observed only with the Fe-containing samples (inset to Fig. 6) and its
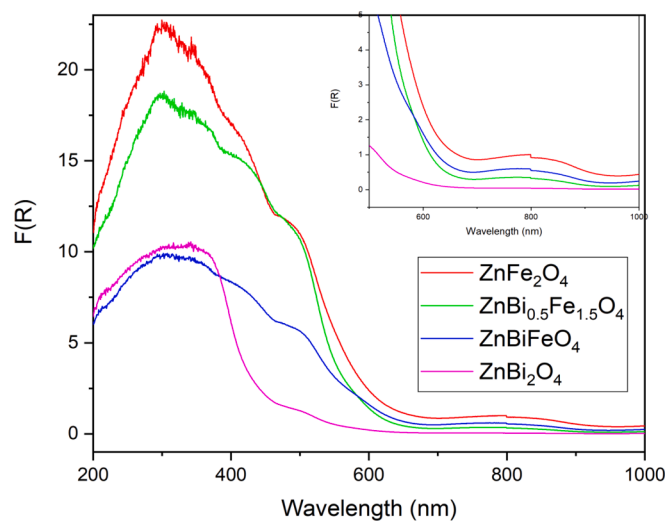
Fig. 6. DR UV–Vis spectra of $ZnBi_xFe_{2-x}O_4$ (x = 0, 0.5, 1, 2) nanomaterials. The inset shows zoom of the spectra in the 500–1000 nm range.

intensity decreased with the Fe content. The band observed at ca. 500 nm with the $ZnBi_2O_4$ sample could not be ascribed to such CF transition (due to Fe^{3+}). The $ZnBi_2O_4$ spectrum is in agreement with a previously reported DR-UV–Vis spectrum of bismuth zinc oxide,[52] whereas the band shape is compatible with some inter-band transitions, likely due to defects and/or metal-to-metal charge transfer transitions. Except for the $ZnBi_2O_4$ sample, all the spectra in Fig. 6 also show a shoulder at ca 430 nm, likely related to Fe: according to the literature the shoulder at 430 nm can be assigned to a charge transfer transition among the d-orbitals of octahedral and tetrahedral Fe^{3+}ions [51].

The Tauc's plot method is used to estimate the energy gap (E_g) of the materials by considering a direct transition process [5]. Tauc's plot is

extrapolated by taking into account the edges in a way that includes the band tailing effect caused by defects or surface states (Figure S2, supporting information). Table 2 lists the average energy gap of ZnBi$_x$Fe$_{2-x}$O$_4$ (x = 0, 0.5, 1, 2) materials, When Bi^{3+} ions are added to the ZnFe$_2$O$_4$ spinel, the E$_g$ decreases for x = 0.5, 1 and then increases for ZnBi$_2$O$_4$, in agreement with the literature values reported for this material, between 2.90 and 3.00 eV [52].

The valence band maximum (E$_V$) of ZnBi$_x$Fe$_{2-x}$O$_4$ (x = 0, 0.5, 1, 2) materials is extracted from XPS valence band spectra and the method is reported in the supporting information, Figure S3. Table 2 reports E$_g$, and E$_V$ together with the computed conduction band minimum E$_C$ (=E$_g$ + E$_V$). Since it is assumed that the materials have a Fermi energy (E$_F$) of '0′ eV, the E$_V$ values are reported negatively.

3.3. Electrochemical characterization

3.3.1. Electroactive area of the sensors

Bare and ZnBi$_x$Fe$_{2-x}$O$_4$ (x = 0, 0.5, 1, 2) sensors are characterized in 50 mL of 4 mM Ferri/ferrocyanide in 0.1 M PB at pH 7 by CV. Cyclic voltammograms at different scan rates (ν) (25 – 150 mV/s in steps of 25 mV/s) are presented in Figure S4 (supporting information). In all the cases, anodic peak currents are varying linearly with the square root of the scan rate as shown in the inset of Figure S4, indicating a diffusion controlled process of reactants at the electrode–electrolyte interface [53,54]. The electroactive area (A) is calculated using the slope of the anodic peak current (I$_{pa}$) versus $\sqrt{\nu}$ by following the Randles-Sevčik equation that is written in the equation (1).[55]

$$I_p = 2.69 \bullet 10^2 A D^{1/2} n^{3/2} \nu^{1/2} \qquad (1)$$

where I$_p$ is the peak current, A is the electroactive area, D is the diffusion coefficient of the electrolyte taken as 6.8 × 10^{-6} cm^2/s,[56] n is the number of electrons participating in the redox reaction. C is the concentration of the redox molecules in the electrolytic solution. The calculated Randles-Sevčik electroactive area (A$_{R-S}$) of the sensors and the real area (A$_R$) (A$_{R-S}$/A$_{Geom}$; A$_{Geom}$ = Geometrical area of the working electrode = 0.12 cm^2) are presented in Table S2 of the supporting information. We observe the increment in the A$_{R-S}$ due to nanostructuration of the working electrode surface. Compared to the bare carbon surface, we expect always a higher area of the sensor due to surface roughness and presence of nanostructured materials. Of course, the electrochemical active area depends on the morphology, orientation, and size of the particles.

3.3.2. Electrochemical impedance spectroscopy (EIS) studies

In order to further understand the electrochemical system, electrochemical impedance spectroscopy (EIS) is performed using the same set up as described above. The related Nyquist plots are fitted with the modified Randles equivalent circuit model presenting R$_s$ (series resistance), R$_{ct}$ (charge transfer resistance), CPE (constant phase element), and Warburg impedance (W). Randles equivalent circuit and the Nyquist plots for all the sensors are reported in Fig. 7. The fitting parameters (R$_s$, R$_{ct}$) are presented in Table S3 in the supporting information. The Nyquist plots showed a typical semi circle at higher frequencies and tend to be linear at lower frequencies indicating the electron transfer limited (R$_{ct}$) and diffusion limited process (W) at the interface [56]. It is observed that the ohmic resistance between the reference and the working electrode R$_s$ has been reduced by the introduction of the

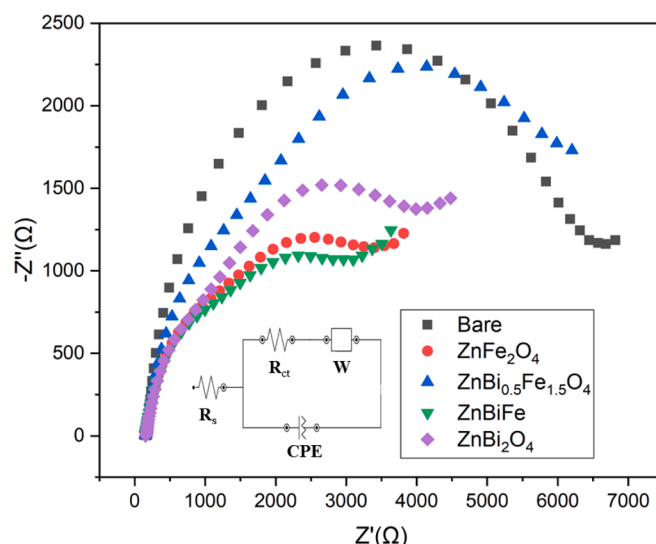**Fig. 7.** Nyquist plots from EIS studies of the bare and ZnBi$_x$Fe$_{2-x}$O$_4$ (x = 0, 0.5, 1, 2) sensors with 4 mM Ferri/ferrocyanide redox probe in 0.1 M PB at pH 7. [Frequency range: 0.1 – 100 kHz with 10 points per decade at an amplitude of 5 mV].

nanostructured spinel materials compared to the bare carbon and similarly the charge transfer resistance (R$_{ct}$) has been significantly reduced by the presence of ZnBi$_x$Fe$_{2-x}$O$_4$ materials showing their superior electrochemical performance with respect to the bare carbon sensor.

3.3.3. Electrochemical sensing of paracetamol

Fig. 8 shows the cyclic voltammograms of bare and ZnBi$_x$Fe$_{2-x}$O$_4$ (x = 0, 0.5, 1, 2) sensors in presence of 1 mM paracetamol in 0.1 M PB at pH 7 at a scan rate (ν) of 100 mV/s. It is evident from Fig. 8 that the ZnBi$_x$Fe$_{2-x}$O$_4$ (x = 0, 0.5, 1, 2) materials-modified sensors have a significantly enhanced electrochemical sensing of paracetamol compared to the bare carbon sensor. The oxidation current decreased with the introduction of Bi(III) into the composition of ZnFe$_2$O$_4$ and decreased further as Bi(III) completely replaced the Fe(III) while the oxidation potential increased. The particle morphology has changed from a spherical-like shape (zinc ferrite) to a patch-like shape with a larger size (zinc bismuthate) as we increased the amount of Bi in ZnFe$_2$O$_4$. This is one of the important factors that impacted the

Table 2
Estimated E$_g$, E$_V$, and E$_C$ of ZnBi$_x$Fe$_{2-x}$O$_4$ (x = 0, 0.5, 1, 2) nanomaterials.

Material	Eg (eV)	Ev (eV)	Ec (eV)
ZnFe$_2$O$_4$	2.58 ± 0.06	−1.87 ± 0.49	0.71 ± 0.55
ZnBi$_{0.50}$Fe$_{1.50}$O$_4$	2.43 ± 0.08	−0.85 ± 0.25	1.58 ± 0.33
ZnBiFeO$_4$	2.40 ± 0.02	−1.29 ± 0.10	1.11 ± 0.12
ZnBi$_2$O$_4$	2.95 ± 0.06	−1.22 ± 0.14	1.73 ± 0.20

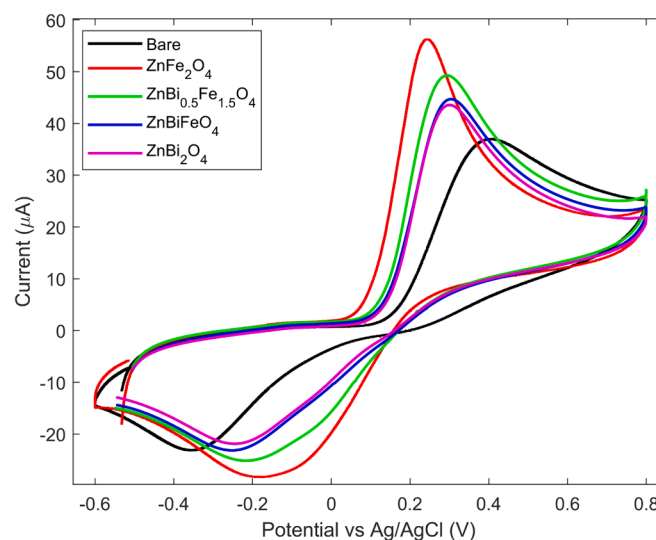**Fig. 8.** Cyclic voltammograms of Bare and ZnBi$_x$Fe$_{2-x}$O$_4$ (x = 0, 0.5, 1, 2) sensors with 1 mM paracetamol in 0.1 M PB at pH 7. (ν = 100 mV/s).

electrochemical performance of the materials. Though the performance has degraded with the introduction of Bi into zinc ferrite, it is significantly better than the performance of bare carbon sensor with an oxidation current increment (>8 µA) and a potential decrement (>100 mV).

3.3.3.1. Effect of scan rate. To evaluate the nature of the electrochemical interface, cyclic voltammetry is performed by varying the scan rate. Scan rate is varied from 50 mV/s to 300 mV/s in increments of 50 mV/s. Fig. 9 (a) and (d) show the cyclic voltammograms of $ZnBi_xFe_{2-x}O_4$ (x = 1, 2) with scan rate while inset figures show the anodic (I_{pa}) and cathodic peak (I_{pc}) currents with respect to $\sqrt{\nu}$ for bare and $ZnBi_xFe_{2-x}O_4$ (x = 0, 1, 2) sensors. The plots are reported in Figure S5, supporting information for $ZnBi_{0.5}Fe_{1.5}O_4$ sensor and our previous work can be referred for bare and zinc ferrite sensors [5]. Table 3 shows the linear regression equations and fitting coefficients of different sensors. We noticed a very good linearity of redox peak currents with $\sqrt{\nu}$, and the position of the redox peaks is changing with the change in the scan rate. An explanation of the effect of the scan rate ν is given in the Randles-Sevčik theory [55,57]. When 'ν' increases, the capacitive current and faradaic current generated by the redox reaction at the interface also increase, contributing to an overall current increase. A freely diffusing quasi-reversible electrochemical system is identified when the peak position varies with 'ν', and the current varies linearly with $\sqrt{\nu}$.

3.3.3.2. Kinetic parameters. The anodic (E_{pa}) and cathodic (E_{pc}) peak positions are evaluated with the scan rate and plotted (Fig. 9 (b) and (e) for $ZnBi_xFe_{2-x}O_4$ (x = 1, 2) sensors) with respect to $\ln(\nu)$. Peak-to-peak separation ($\Delta E_p = E_{pa}-E_{pc}$) is calculated and plotted (Fig. 9 (c) and (f) for $ZnBi_xFe_{2-x}O_4$ (x = 1, 2) sensors) against the $\ln(\nu)$ for different sensors. Figure S5, supporting information shows the plots for $ZnBi_{0.5}Fe_{1.5}O_4$ sensor and our previous work can be referred to for bare and zinc ferrite sensors [5]. We identified a linear variation of redox peak potentials and ΔE_p with $\ln(\nu)$ and the linear regression equations with their coefficients are reported in Table 4 and 5, respectively. Since redox peak currents

and redox peak positions follow a linear relationship with respect to $\sqrt{\nu}$ and $\ln(\nu)$ respectively, the Laviron model[58] can be applied to evaluate the electron transfer rate coefficient (α). Laviron model describes the redox peak positions E_{pc} and E_{pa} as

Table 3

I_{pa}, I_{pc} regression equations of the bare and the $ZnBi_xFe_{2-x}O_4$ (x = 0, 0.5, 1, 2) sensors.

Sensor	I_{pa}	R^2	I_{pc}	R^2
Bare	$2.82\sqrt{\nu} + 6.35$	0.998	$-2.26\sqrt{\nu} + 8.93$	0.999
$ZnFe_2O_4$	$5.86\sqrt{\nu} + 0.87$	0.999	$-3.27\sqrt{\nu} + 4.35$	0.991
$ZnBi_{0.5}Fe_{1.5}O_4$	$4.93\sqrt{\nu} + 1.17$	0.995	$-3.35\sqrt{\nu} + 9.24$	0.958
$ZnBiFeO_4$	$4.48\sqrt{\nu} - 0.32$	0.985	$-2.71\sqrt{\nu} + 6.43$	0.978
$ZnBi_2O_4$	$3.69\sqrt{\nu} + 5.28$	0.997	$-1.82\sqrt{\nu} + 1.98$	0.987

Table 4

E_{pa}, E_{pc} regression equations for bare and $ZnBi_xFe_{2-x}O_4$ (x = 0, 0.5, 1, 2) sensors.

Sensor	E_{pa}	R^2	E_{pc}	R^2
Bare	$41.5\ln(\nu) + 216.1$	0.973	$-33.3\ln(\nu) - 189.3$	0.996
$ZnFe_2O_4$	$26.4\ln(\nu) + 127.3$	0.975	$-90.2\ln(\nu) - 278.3$	0.996
$ZnBi_{0.5}Fe_{1.5}O_4$	$18.5\ln(\nu) + 218.5$	0.962	$-65.7\ln(\nu) + 155.6$	0.987
$ZnBiFeO_4$	$28.9\ln(\nu) + 160$	0.951	$-57.5\ln(\nu) + 82.3$	0.993
$ZnBi_2O_4$	$20.3\ln(\nu) + 216.8$	0.988	$-47.3\ln(\nu) + 18.2$	0.992

Table 5

ΔE_p regression equations for bare and $ZnBi_xFe_{2-x}O_4$ (x = 0, 0.5, 1, 2) sensors.

Sensor	ΔE_p	R^2
Bare	$74.81\ln(\nu) + 405.47$	0.991
$ZnFe_2O_4$	$116.64\ln(\nu) - 151.01$	0.999
$ZnBi_{0.5}Fe_{1.5}O_4$	$84.16\ln(\nu) + 62.85$	0.987
$ZnBiFeO_4$	$86.51\ln(\nu) + 77.71$	0.989
$ZnBi_2O_4$	$67.61\ln(\nu) + 198.62$	0.996

Fig. 9. (a), (d) Cyclic voltammograms with scan rate from 50 – 300 mV/s (step of 50 mV/s) with 1 mM paracetamol in 0.1 M PB at pH 7. Inset shows the redox currents (I_{pa}: anodic peak current and I_{pc}: cathodic peak current) variation with $\sqrt{\nu}$. (b), (e) Variation of peak positions with $\ln(\nu)$ (E_{pa}: anodic peak potential and E_{pc}: cathodic peak potential). (c), (f) Peak to peak separation (ΔE_p) with respect to $\ln(\nu)$ for $ZnBi_2O_4$ and $ZnBiFeO_4$ sensors, respectively.

$$E_{pc} = E^0 - \left(\frac{RT}{\alpha nF}\right)ln\left[\frac{\alpha}{|m|}\right] \qquad (2)$$

$$E_{pa} = E^0 + \left(\frac{RT}{(1-\alpha)nF}\right)ln\left[\frac{(1-\alpha)}{|m|}\right] \qquad (3)$$

where $m = (RT/F)(k/n\nu)$, '*T*' is the absolute temperature in Kelvin, '*F*' is the Faraday constant, '*R*' is the universal constant for gas, '*n*' is the number of electrons engaged in the redox reaction, and '$E^{0\prime}$' is the standard surface potential.

The slopes of E_{pa} and E_{pc} vs $ln(\nu)$ fitting lines are used to calculate the value of "α". We have α, $n = 2$, and the system is a quasi-reversible one hence the ΔE_p value is chosen at $\nu = 100$ mV/s.

$$ln(k) = \alpha ln(1-\alpha) + (1-\alpha)ln(\alpha) - ln\left(\frac{RT}{nF\nu}\right) - \alpha(1-\alpha)\frac{nF\Delta E_p}{RT} \qquad (4)$$

Equation (4), the Laviron equation for '*k*', is used to derive the kinetic rate constant '*k*'. The calculated electron transfer rate coefficient 'α', ΔE_p, and kinetic rate constant '*k*' for bare and $ZnBi_xFe_{2-x}O_4$ (x = 0, 0.5, 1, 2) sensors are listed in Table 6. It is observed that 'α' has decreased from bare to zinc ferrite sensor and increased as we increase the amount of Bi in the composition of zinc ferrite. The same effect has been observed with the peak-to-peak separation of the sensors whereas the '*k*' has increased significantly from bare to zinc ferrite and has decreased when the amount of Bi(III) increase. This analysis proves that the modified sensors have shown a significant improvement in the reaction rate at the interface compared to the bare carbon sensor with zinc ferrite, without any presence of Bi(III), being the best sensor. The insertion of Bi(III) has shown a very significant effect on the sensor performance in terms of reaction rate at the interface.

3.3.3.3. Sensitivity and limit of detection. At a set scan rate, cyclic voltammograms are recorded at various paracetamol concentrations. Each sensor is calibrated after the oxidation current is gathered and averaged over three assessments at each concentration. The calibration of the different sensors is reported in Fig. 10. The sensitivity of the sensors is reported by taking the slope of the respective calibration of sensors in Table 7. The sensitivity is more than two-fold increased for the zinc ferrite sensor (37.8 ± 0.2 µA/mM) with respect to the bare one (16.7 ± 0.9 µA/mM). As the content of Bi^{3+} ions increased the morphology changed from spherical to platelike shape and the particle size increased. Moreover, the crystal structure of $ZnFe_2O_4$ was modified, and the higher ionic size of Bi^{3+} compared to Fe^{3+} affected the strain. These changes due to the introduction of the Bi^{3+} ions affected the electrochemical sensor performance leading to a decrease in the sensitivity with the increase in Bi^{3+} ions content.

XRD showed (Fig. 3) the presence of two different phases, namely, zinc ferrite and zinc bismuthate, along with some secondary phases such as ZnO and Fe_2O_3. Unlike our previous works, [5,18] we obtained a dual spinel phase instead of a solid solution of two spinel materials with a single phase. This might be one of the reasons why we observed two distinct morphologies in Fig. 2(b-d) of FESEM images where spherical shape can be ferrite and patch-like shape can be bismuthate. This heavily affects electrochemical properties as we are witnessing the effect of two different materials instead of a single material when we have both Bi(III) and Fe(III) in the material. This also indicates that instead of

Table 6

α, ΔE_p, and *k* of the bare and $ZnBi_xFe_{2-x}O_4$ (x = 0, 0.5, 1, 2) sensors.

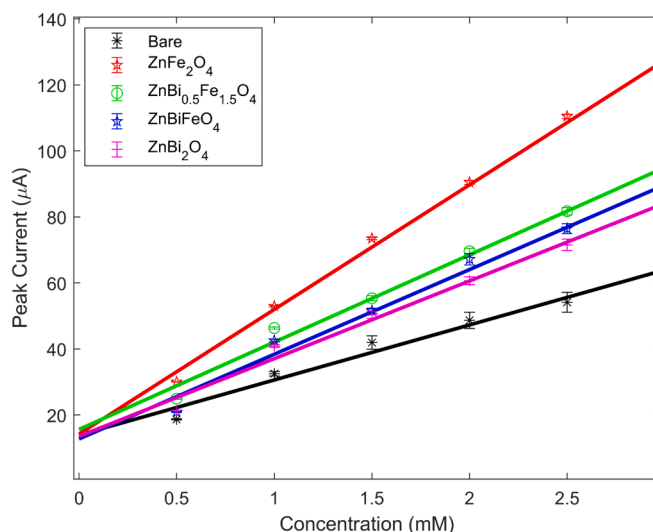| Sensor	α	ΔE_p (mV)	*k* (ms^{-1})
Bare	0.54 ± 0.01	746 ± 5	(2.2 ± 0.2) x 10^{-3}
$ZnFe_2O_4$	0.23 ± 0.02	386 ± 2	13.1 ± 2.8
$ZnBi_{0.50}Fe_{1.50}O_4$	0.24 ± 0.01	438 ± 4	5.6 ± 0.6
$ZnBiFeO_4$	0.30 ± 0.02	479 ± 3	1.3 ± 0.2
$ZnBi_2O_4$	0.32 ± 0.01	532 ± 12	0.45 ± 0.16

Fig. 10. Calibration of bare and $ZnBi_xFe_{2-x}O_4$ (x = 0, 0.5, 1, 2) sensors for paracetamol (0.5 to 3 mM) in 0.1 M PB at pH 7.

Table 7

The sensitivity and limit of detection of the bare and $ZnBi_xFe_{2-x}O_4$ (x = 0, 0.5, 1, 2) sensors.

Sensor	Sensitivity (µA/mM)	R^2	LOD (µM)
Bare	16.7 ± 0.9	0.975	3.26 ± 0.17
$ZnFe_2O_4$	37.8 ± 0.2	0.995	7.94 ± 0.04
$ZnBi_{0.5}Fe_{1.5}O_4$	26.5 ± 0.4	0.988	2.36 ± 0.04
$ZnBiFeO_4$	25.6 ± 0.8	0.980	2.26 ± 0.07
$ZnBi_2O_4$	23.5 ± 0.6	0.986	7.35 ± 0.02

inserting Bi(III) into the crystal structure of zinc ferrite, we have produced two different materials with different behaviors at the electrochemical interface. Zinc ferrite showed better sensitivity while zinc bismuthate showed lower sensitivity whereas the combination showed a slightly higher sensitivity compared to the zinc bismuthate. High-resolution XPS spectra showed that the insertion of Bi(III) has affected the spinel structure where Fe(III) occupies both the 'Td' and 'Oh' sites along with Bi, as shown by DR UV–Vis spectroscopy. This modified the normal spinel structure into a mixed spinel structure. As we previously demonstrated, the type of spinel structure plays a crucial role in the electrochemical sensing performance due to different conductive mechanisms [5].

To compute the limit of detection (LOD) we used the well-assessed formula (LOD) = KD/S. K stands for the statistical confidence level, which is set at '3', D for the standard deviation of the blank data, and S for the sensor's sensitivity. Table 7 presents the LOD for each sensor. Among the sensors in the current investigation, $ZnFe_2O_4$ has the greatest LOD of 7.94 ± 0.04 µM, while the $ZnBiFeO_4$ sensor shows the lowest LOD of 2.26 ± 0.07 µM.

The current work is compared with the previously reported work for electrochemical sensing of paracetamol by using spinel oxide-based nanomaterials. The different synthesis methods, electrochemical characterization techniques used, linear range, limit of detection of different electrochemical sensors for paracetamol are reported in Table 8. Since the linear range and studied conditions of the sensors are different it is difficult to directly compare the performances of the current materials with those previously reported in Table 8.

Other important features of electrochemical sensors are the stability, repeatability, and reproducibility. We observed very stable electrochemical results with a standard deviation of around 1 µA within a span of 3 weeks in oxidation peak current of paracetamol using our modified sensors. Usually non-enzymatic screen-printed electrochemical sensors

Table 8
Electrochemical sensing of paracetamol by different spinel metal oxides-based sensors.

Sensor	Method	Technique	Linear range (µM)	LOD (µM)	Reference
CoFe$_2$O$_4$	Combustion	DPV	3–200	0.25	[34]
MnFe$_2$O$_4$	Combustion	CV	1000–5000	–	[30]
NiFe$_2$O$_4$	Hydrothermal	DPV	1–90	0.49	[31]
NiFe$_2$O$_4$	Combustion	CV	500–3000	6.93	[5]
NiFe$_2$O$_4$	Thermal treatment	DPV	0.6–8.5	0.08	[32]
ZnFe$_2$O$_4$	Hydrothermal	DPV	0–500	0.29	[33]
ZnFe$_2$O$_4$	Combustion	CV	500–3000	7.94	This work
ZnBiFeO$_4$	Combustion	CV	500–3000	2.26	This work
ZnBi$_2$O$_4$	Combustion	CV	500–3000	7.35	This work

provide very stable results [59,60]. The repeatability of the sensors modified with ZnFe$_2$O$_4$ and ZnBi$_2$O$_4$ sensors is studied by performing 5 measurements under the same conditions and they have a relative standard error mean (R$_{sem}$) of 1.07 % and 0.9 %, respectively. The reproducibility of ZnFe$_2$O$_4$ and ZnBi$_2$O$_4$ sensors is checked by characterizing three different sensors of each type and found to have a R$_{sem}$ of 1.58 % and 2.1 %, respectively.

3.3.3.4. Interference tests. To understand the effect interferences with paracetamol, the best sensor in this study (ZnFe$_2$O$_4$ sensor) is characterized. Paracetamol (100 µM) solution is prepared in 0.1 M PB at pH 7 along with 50 µM of ascorbic acid (AA), 50 µM of uric acid (UA). A freshly prepared ZnFe$_2$O$_4$ sensor is used to perform the CV measurements to detect the presence of paracetamol in presence of AA and UA. It is observed from Fig. 11 (cyclic voltammogram in red) that the redox reaction of paracetamol is clearly distinguishable (oxidation peak at 287 mV) from the interference of AA (oxidation around 125 mV) and UA (usually occurs around 350 mV) seemed to be not oxidized by the sensor hence we observe no peak around or above 350 mV. The sensor is also tested for the interference study of the presence of ions K$^+$, Na$^+$, Mg^{2+} and Cl$^-$ by adding 5 mM KCL, 5 mM NaCl, and 5 mM MgCl$_2$ to the 100 µM paracetamol solution in 0.1 M PB at pH 7. We clearly observed the effect of the presence of inorganic ions in Fig. 11 (cyclic voltammogram in black) as the oxidation potential has increased from 287 mV to 377 mV and oxidation peak current has been reduced from 9.9 µA to 6.03 µA proving the significant effects on the sensor surface.
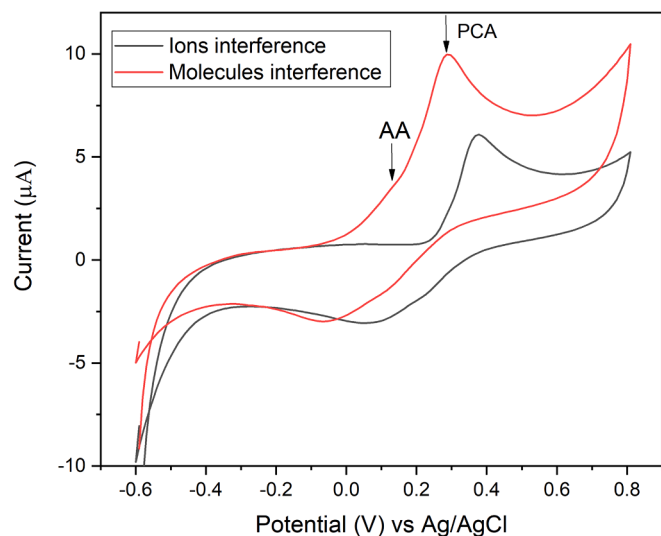
3.4. Energy bands and redox potential mapping

Inspired by Burello and Worth's theoretical predictive model [62,63] and some of the previous work reported in the literature, [5,20,35,64] we have used the band energy levels of the nanomaterials to predict the type of electron transfer. The estimated conduction band energy minimum E$_C$ and valence band energy maximum E$_V$ are compared to the experimental redox potentials of paracetamol as shown in Fig. 12. We observed that only the E$_C$ of ZnFe$_2$O$_4$ overlaps with the redox potential of paracetamol, indicating direct electron transfer at the electrochemical interface between the nanomaterial surface and paracetamol. Though there is no overlap between E$_C$ and redox potential of paracetamol for the bismuth-containing sensors, we have observed a good improvement in electrochemical sensitivity and rate constant compared to the bare carbon sensor. In these cases, it is possible to have an indirect electron transfer with the help of surface states/defects of the nanomaterials. XRD has confirmed the presence of ZnO, Fe$_2$O$_3$, and Raman has shown the presence of cubic phase Bi$_2$O$_3$; hence, this type of indirect electron transfer is usually a surface state mediated transfer. This could be the main reason for zinc ferrite to produce the highest sensitivity and faster reactions at the electrochemical interface whereas the other cases have lower sensitivity and slower reaction rates due to the involvement of surface states with multiple transfer rates giving rise to an average effect by the end of the electron transfer.

4. Conclusions

In this work, we synthesized ZnBi$_x$Fe$_{2-x}$O$_4$ (x = 0, 0.5, 1, 2) nanomaterials using a simple self-combustion synthesis technique. The main aim of this work is to understand the effects of ionic size on nanomaterials performance in electrochemical sensing applications. To be able to understand the effect of Bi^{3+} ions on the electrochemical sensing performance of ZnFe$_2$O$_4$ nanoparticles, cyclic voltammetry is used to successfully characterise five different sensors.

All the studied ZnBi$_x$Fe$_{2-x}$O$_4$ spinel nanomaterials tailored sensors have a sensitivity higher than the bare sensor with a lower ΔE$_p$ and a higher 'k'. ZnFe$_2$O$_4$ sensor has the highest capability in maximizing the sensitivity and rate constant leading to faster electrochemical reactions at the nanomaterial and paracetamol interface. It is difficult to make a direct comparison with different morphologies and particle sizes ranging from the nano-scale to sub-micrometer scale from material to
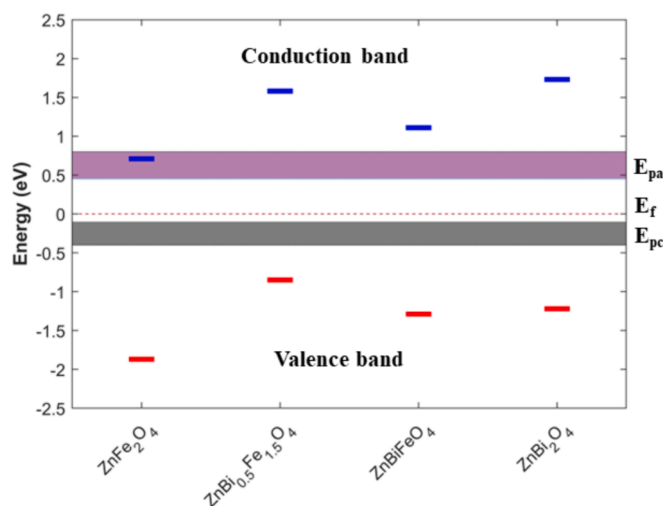
Fig. 11. Study of the interference effects of ZnFe$_2$O$_4$ sensor in 100 µM paracetamol in 0.1 M PB at pH 7 with 50 µM ascorbic acid (AA) and 50 µM uric acid (UA) (red curve) and with 5 mM KCl, 5 mM NaCl, and 5 mM MgCl$_2$ (black curve). Cyclic voltammograms at a scan rate of 100 mV/s.

Fig. 12. Mapping of energy bands of ZnBi$_x$Fe$_{2-x}$O$_4$ (x = 0, 0.5, 1, 2) nanomaterials with redox potential (E$_{pa}$: Anodic peak potential and E$_{pc}$: Cathodic peak potential) of paracetamol in predicting electron transfer at the electrochemical interface. E$_f$ is the Fermi energy level of nanomaterials assumed to be at zero eV.

material whereas we have nanoparticles and a combined spinel phase with chromium substitution. The energy gap and bands edge energy positions are used to predict the type of electron transfer at the interface along with the redox potentials of paracetamol. The change in the composition obtained by inserting Bi(III) and the particle size have affected the band gap that in turn affected the electrochemical performance. Overall, the spinel-based nanomaterials have enhanced electrochemical performance compared to the bare carbon sensors.

The rational design of spinel-based nanomaterials by suitable methods could be extended in the detection of O_2, pH, and different types of drugs in biomedical applications.

CRediT authorship contribution statement

Mallikarjun Madagalam: Writing – original draft, Visualization, Methodology, Investigation, Formal analysis, Data curation, Conceptualization. **Michele Rosito:** Writing – review & editing, Resources, Formal analysis. **Nicola Blangetti:** Resources, Investigation, Formal analysis. **Marco Etzi:** Writing – review & editing, Formal analysis, Data curation. **Elisa Padovano:** Writing – review & editing, Resources. **Barbara Bonelli:** Writing – review & editing, Resources. **Sandro Carrara:** Writing – review & editing, Supervision. **Alberto Tagliaferro:** Writing – review & editing, Validation, Supervision. **Mattia Bartoli:** Writing – review & editing, Validation, Supervision, Resources, Conceptualization.

Declaration of competing interest

The authors declare that they have no known competing financial interests or personal relationships that could have appeared to influence the work reported in this paper.

Data availability

Data will be made available on request.

Appendix A. Supplementary data

Supplementary data to this article can be found online at https://doi.org/10.1016/j.apsusc.2024.160870.

References

[1] J. Kim, W. Ko, J.M. Yoo, V.K. Paidi, H.Y. Jang, M. Shepit, J. Lee, H. Chang, H. S. Lee, J. Jo, B.H. Kim, S.-P. Cho, J. van Lierop, D. Kim, K.-S. Lee, S. Back, Y.-E. Sung, T. Hyeon, Advanced Materials 34 (2022) 2107868.
[2] H. Kim, D.-H. Seo, H. Kim, I. Park, J. Hong, K.-Y. Park, K. Kang, Chem. Mater. 24 (2012) 720.
[3] K. Lee, D.A. Ruddy, G. Dukovic, N.R. Neale, J. Mater. Chem. A 3 (2015) 8115.
[4] Q. Zhang, Y. Hu, H. Wu, X. Zhao, M. Wang, S. Wang, R. Feng, Q. Chen, F. Song, M. Chen, P. Liu, ACS Nano 17 (2023) 1485.
[5] M. Madagalam, M. Bartoli, M. Rosito, N. Blangetti, M. Etzi Coller Pascuzzi, E. Padovano, B. Bonelli, S. Carrara, A. Tagliaferro, Small Structures 4 (2023) 2300163.
[6] J.M. Gonçalves, L.V. de Faria, A.B. Nascimento, R.L. Germscheidt, S. Patra, L. P. Hernández-Saravia, J.A. Bonacin, R.A.A. Munoz, L. Angnes, Analytica Chimica Acta 1233 (2022) 340362.
[7] R. Suresh, R. Rajendran, P.S. Kumar, D.-V.-N. Vo, L. Cornejo-Ponce, Chemosphere 274 (2021) 129734.
[8] H. Gao, Y. Li, H. Zhao, J. Xiang, Y. Cao, Electrochimica Acta 262 (2018) 241.
[9] A.N. Alqarni, E. Cevik, M.A. Almessiere, A. Baykal, M.A. Gondal, M. Hassan, A. Bozkurt, A. Iqbal, S.M. Asiri, Y. Slimani, Journal of Physics and Chemistry of Solids 177 (2023) 111288.
[10] S. Li, X. Zhou, G. Fang, G. Xie, X. Liu, X. Lin, H.-J. Qiu, A.C.S. Appl, Energy Mater. 3 (2020) 7710.
[11] F.M. Courtel, H. Duncan, Y. Abu-Lebdeh, I.J. Davidson, J. Mater. Chem. 21 (2011) 10206.
[12] C. Li, X. Han, F. Cheng, Y. Hu, C. Chen, J. Chen, Nature Communications 6 (2015) 7345.
[13] C.H. Jiang, S.X. Dou, H.K. Liu, M. Ichihara, H.S. Zhou, Journal of Power Sources 172 (2007) 410.
[14] C.R. Vestal, Z.J. Zhang, Nano Lett. 3 (2003) 1739.
[15] F. Moradnia, S. Taghavi Fardood, A. Ramazani, S. Osali, I. Abdolmaleki, Micro & Nano Letters 15 (2020) 674.
[16] D.S. Mathew, R.-S. Juang, Chemical Engineering Journal 129 (2007) 51.
[17] H.L. Andersen, M. Saura-Múzquiz, C. Granados-Miralles, E. Canévet, N. Lock, M. Christensen, Nanoscale 10 (2018) 14902.
[18] M. Madagalam, M. Bartoli, S. Carrara, A. Tagliaferro. *2023,* IEEE SENSORS, 2023, pp. 1–4, https://doi.org/10.1109/SENSORS56945.2023.10325135.
[19] M. Madagalam, M. Bartoli, S. Carrara, A. Tagliaferro, *2023 IEEE BioSensors Conference (BioSensors),* **2023,** pp. 1–4. 10.1109/BioSensors58001.2023.10280910.
[20] X. Kang, J. Wang, H. Wu, J. Liu, I.A. Aksay, Y. Lin, Talanta 81 (2010) 754.
[21] R.M. de Carvalho, R.S. Freire, S. Rath, L.T. Kubota, Journal of Pharmaceutical and Biomedical Analysis 34 (2004) 871.
[22] M. Li, L. Jing, Electrochimica Acta 52 (2007) 3250.
[23] M. Madagalam, M. Bartoli, A. Tagliaferro, S. Carrara, IEEE Sensors Journal 21 (2021) 11155.
[24] M. Dinamani, B.S. Surendra, H.C.A. Murthy, N. Basavaraju, V.V. Shanbhag, Environmental Nanotechnology, Monitoring & Management 20 (2023) 100822.
[25] B.S. Surendra, K. Gurushantha, K.S. Ananthraju, M. Rudresh, N. Basavaraju, N. Raghavendra, A.A. Jahagirdar, H.M. Somashekar, H.C.A. Murthy, New J. Chem. 47 (2023) 3978.
[26] N. Basavaraju, S.C. Prashantha, B.S. Surendra, T.R.S. Shekhar, M.R.A. Kumar, C. R. Ravikumar, N. Raghavendra, T.S. Shashidhara, Environmental Nanotechnology, Monitoring & Management 16 (2021) 100581.
[27] M. Mylarappa, N. Raghavendra, B.S. Surendra, K.N.S. Kumar, S. Kantharjau, Applied Surface Science Advances 10 (2022) 100268.
[28] M. Giridhar, B.C. Manjunath, B.S. Surendra, K.N. Harish, S.C. Prashantha, T. Kiran, B. Uma, H.C.A. Murthy, Scientific Reports 13 (2023) 17821.
[29] N. Raghavendra, H.P. Nagaswarupa, T.R.S. Shekhar, M. Mylarappa, B.S. Surendra, S.C. Prashantha, C.R. Ravikumar, M.R.A. Kumar, N. Basavaraju, Applied Surface Science Advances 5 (2021) 100103.
[30] S. Meena, K.S. Ananthraju, S. Malini, A. Dey, L. Renuka, S.C. Prashantha, Y. S. Vidya, Ceramics International 47 (2021) 14723.
[31] M. Nouri, M. Rahimnejad, G. Najafpour, A.A. Moghadamnia, Microchimica Acta 187 (2020) 315.
[32] M. Kumar, B.E.K. Swamy, C. Sravanthi, C.M.P. Kumar, G.K. Jayaprakash, Materials Chemistry and Physics 284 (2022) 126087.
[33] N.T. Anh, L.M. Tung, L.K. Vinh, N. Van Quy, O. Van Hoang, N.X. Dinh, A.-T. Le, Nanoscale Adv. 6 (2024) 256.
[34] Y. Kumar, P. Pramanik, D.K. Das, Heliyon 5 (2019) e02031.
[35] K.D. Rajan, D. Srinivasan, P.P. Gotipamul, S. Khanna, S. Chidambaram, M. Rathinam, Materials Science and Engineering: B 285 (2022) 115929.
[36] A. Habibi-Yangjeh, M. Pirhashemi, S. Ghosh, Journal of Alloys and Compounds 826 (2020) 154229.
[37] V.-H. Nguyen, M. Mousavi, J.B. Ghasemi, Q.V. Le, S.A. Delbari, A. Sabahi Namini, M. Shahedi Asl, M. Shokouhimehr, M. Mohammadi, J. Phys. Chem. C 124 (2020) 27519.
[38] A.C.F.M. Costa, E. Tortella, M.R. Morelli, M. Kaufman, R.H.G.A. Kiminami, Journal of Materials Science 37 (2002) 3569.
[39] B.D. Prasad, H. Nagabhushana, K. Thyagarajan, B.M. Nagabhushana, D. M. Jnaneshwara, S.C. Sharma, C. Shivakumara, N.O. Gopal, S.-C. Ke, R.P. S. Chakradhar, Journal of Magnetism and Magnetic Materials 358–359 (2014) 132.
[40] V.S. Veena, H.J.A. Yadav, S.P. Kubrin, M. Ubaidullah, A.-M.-A. Enizi, B. Pandit, H. S. Gill, K. Manjunatha, V.J. Angadi, Journal of Magnetism and Magnetic Materials 571 (2023) 170561.
[41] M.Z. Shoushtari, A. Emami, S.E.M. Ghahfarokhi, Journal of Magnetism and Magnetic Materials 419 (2016) 572.
[42] N.S. Kumar, Journal of Physics: Conference Series 1495 (2020) 012015.
[43] L.H. Ahrens, Geochimica et Cosmochimica Acta 2 (1952) 155.
[44] O. Depablos-Rivera, A. Martínez, S.E. Rodil, Journal of Alloys and Compounds 853 (2021) 157245.
[45] M. Šćepanović, M. Grujić-Brojčin, K. Vojisavljević, S. Bernik, T. Srećković, Journal of Raman Spectroscopy 41 (2010) 914.
[46] K. Xu, L. Zhang, A. Godfrey, D. Song, W. Si, Y. Zhao, Y. Liu, Y. Rao, H. Zhang, H.-A. Zhou, W. Jiang, W. Wang, Z. Cheng, J. Zhu, Proceedings of the National Academy of Sciences 118 (2021).
[47] M. Etzi Coller Pascuzzi, A.J.W. Man, A. Goryachev, J.P. Hofmann, E.J.M. Hensen, Catal Sci. Technol. 10 (2020) 5593.
[48] M. Etzi Coller Pascuzzi, M. van Velzen, J.P. Hofmann, E.J.M. Hensen, ChemCatChem 13 (2021) 459.
[49] K. Dahm, D. Dahm, *Principles of Diffuse Reflectance Spectroscopy,* **2021.**
[50] X. Xu, A.K. Azad, J.T.S. Irvine, Catalysis Today 199 (2013) 22.
[51] K.W. Blazey, Journal of Applied Physics 45 (2003) 2273.
[52] N.T.M. Tho, D.N.N. Khanh, N.Q. Thang, Y.-I. Lee, N.T.K. Phuong, Environmental Science and Pollution Research 27 (2020) 11127.
[53] N.G. Tsierkezos, U. Ritter, Journal of Solid State Electrochemistry 14 (2010) 1101.
[54] L. Weber, K. Kloeckner, U. Ritter, P. Scharff, Russian Journal of Electrochemistry 45 (2009) 1145.
[55] A.J. Bard, L.R. Faulkner, Electrochemical methods fundamentals and applications, Wiley, Newyork, NY, USA, 2001.
[56] M.H. de Sá, C.M. Pereira, Electrochimica Acta 489 (2024) 144158.
[57] R.S. Nicholson, Analytical Chemistry 37 (1965) 1351.
[58] E. Laviron, Journal of Electroanalytical Chemistry and Interfacial Electrochemistry 101 (1979) 19.
[59] S. Søpstad, E.A. Johannessen, F. Seland, K. Imenes, Electrochimica Acta 287 (2018) 29.

[60] X. Liu, Y. Yao, Y. Ying, J. Ping, TrAC Trends in Analytical Chemistry 115 (2019) 187.

[62] E. Burello, A.P. Worth, Nanotoxicology 5 (2011) 228.

[63] E. Burello, A.P. Worth, Wires Nanomedicine and Nanobiotechnology 3 (2011) 298.

[64] H. Zhang, Z. Ji, T. Xia, H. Meng, C. Low-Kam, R. Liu, S. Pokhrel, S. Lin, X. Wang, Y.-P. Liao, M. Wang, L. Li, R. Rallo, R. Damoiseaux, D. Telesca, L. Mädler, Y. Cohen, J. I. Zink, A.E. Nel, ACS Nano 6 (2012) 4349.